STATIC AND IMPULSIVE MODELS OF SOLAR ACTIVE REGIONS

S. Patsourakos[1] AND J. A. Klimchuk[2]

Naval Research Laboratory, Space Science Division, Washington, DC 20375; patsourakos@nrl.navy.mil

ABSTRACT

The physical modeling of active regions (ARs) and of the global corona is receiving increasing interest lately. Recent attempts to model ARs using static equilibrium models were quite successful in reproducing AR images of hot soft X-ray (SXR) loops. They however failed to predict the bright extreme-ultraviolet (EUV) warm loops permeating ARs: the synthetic images were dominated by intense footpoint emission. We demonstrate that this failure is due to the very weak dependence of loop temperature on loop length which cannot simultaneously account for both hot and warm loops in the same AR. We then consider time-dependent AR models based on nanoflare heating. We demonstrate that such models can simultaneously reproduce EUV and SXR loops in ARs. Moreover, they predict radial intensity variations consistent with the localized core and extended emissions in SXR and EUV AR observations, respectively. We finally show how the AR morphology can be used as a gauge of the properties (duration, energy, spatial dependence, and repetition time) of the impulsive heating.

Subject headings: hydrodynamics — Sun: corona

1. INTRODUCTION

Modeling ensembles of coronal loops in active regions (ARs) or over the full Sun is a rapidly emerging new field in the study of the solar corona. Such studies attempt to reproduce generic properties of ARs and of the global corona such as space-integrated intensities and overall morphology. This allows for the determination of various properties of coronal heating such as its dependence on loop length and magnetic field, thereby testing coronal heating mechanisms. Moreover, such studies eliminate potential selection effects which may enter into studies of individual loops. Finally, AR and global coronal models pave the way for the construction of physics-based models of the extreme-ultraviolet (EUV) and soft X-ray (SXR) irradiance, an important contributor to space weather conditions.

The majority of the attempted AR and global coronal models were based on static equilibrium coronal loop models produced with steady heating (Schrijver et al. 2004; Mok et al. 2005; Warren & Winebarger 2006; Lundquist et al. 2008). They were quite successful at reproducing the general appearance of the corona in hot emissions (>3 MK) observed in the SXR by the Soft X-Ray Telescope (SXT) on *Yohkoh*. However, synthetic EUV images from the static models did not show evidence of the warm loops seen in the real observations, but instead were dominated by intense footpoint (moss) emission. Steady heating that is highly concentrated near the coronal base can produce time-dependent behavior called thermal nonequilibrium. This gives rise to transient EUV loops (Mok et al. 2008; Klimchuk et al. 2007), but whether their properties are fully consistent with observations has yet to be determined.

Most theories of coronal heating predict that energy is released impulsively on individual flux strands (Klimchuk 2006). This includes both AC (wave) and DC (reconnection type) heating. Following this paradigm coronal loops are viewed as ensembles of unresolved, impulsively heated strands. A very promising idea first proposed by Parker (1988) is that the coronal field becomes tangled on small scales due to the random footpoint motions associated with turbulent photospheric convection. Current sheets develop at the interfaces between individual misaligned strands, and it has recently been shown that an explosive instability called the secondary instability occurs when the misalignment angle reaches a critical value (Dahlburg et al. 2005). This may be the physical nature of the nanoflares postulated by Parker. The heating function we have used in our simulations is appropriate to nanoflares that are initiated at a critical angle. We note that the upward Poynting flux associated with observed photospheric field strengths and observed photospheric velocities is consistent with coronal heating requirements (e.g., Abramenko et al. 2006), but the efficiency of field line tangling is only now being addressed quantitatively with high-resolution magnetogram movies from *Hinode*. We also note that direct observations of the kinds of nanoflares we are discussing are scarce (Katsukawa & Tsuneta 2001). The small distinct brightenings that are sometimes called nanoflares are much different from the unresolved energy releases on long field lines that we consider here.

But why do static equilibrium models fail to reproduce the coronal emission patterns in the EUV? Can impulsive heating models do any better? And how can AR morphology be used to infer the properties of impulsive heating? With this paper we address these important questions.

2. AR SIMULATIONS

For the calculations reported in this paper we use the zero-dimensional hydrodynamic loop model we call enthalpy-based thermal evolution of loops (EBTEL), described in Klimchuk et al. (2008). For a given temporal profile of the heating EBTEL calculates the temporal evolution of the spatially averaged temperature, density, and pressure along the loop. It also provides the differential emission measure distribution [DEM(T)] for both the coronal and footpoint (i.e., transition region) sections of the loop. For steady heating, static equilibrium solutions are calculated. EBTEL is capable of relatively accurately mimicking complex one-dimensional hydrodynamic simulations, with however much less demands in terms of CPU time, which makes it particularly useful for parametric investigations of multitudes of loops. We

[1] Also at: Center for Earth Observing and Space Research, Institute for Computational Sciences–College of Science, George Mason University, Fairfax, VA 22030.

[2] Current address: NASA Goddard Space Flight Center, Code 671, Greenbelt, MD 20771.

1. REPORT DATE **DEC 2008**	2. REPORT TYPE	3. DATES COVERED **00-00-2008 to 00-00-2008**

4. TITLE AND SUBTITLE	5a. CONTRACT NUMBER
Static And Impulsive Models Of Solar Active Regions	5b. GRANT NUMBER
	5c. PROGRAM ELEMENT NUMBER
6. AUTHOR(S)	5d. PROJECT NUMBER
	5e. TASK NUMBER
	5f. WORK UNIT NUMBER

7. PERFORMING ORGANIZATION NAME(S) AND ADDRESS(ES) **Naval Research Laboratory,Space Science Division,Washington,DC,20375**	8. PERFORMING ORGANIZATION REPORT NUMBER

9. SPONSORING/MONITORING AGENCY NAME(S) AND ADDRESS(ES)	10. SPONSOR/MONITOR'S ACRONYM(S)
	11. SPONSOR/MONITOR'S REPORT NUMBER(S)

12. DISTRIBUTION/AVAILABILITY STATEMENT
Approved for public release; distribution unlimited

13. SUPPLEMENTARY NOTES
The Astrophysical Journal, 689:1406Y1411, 2008 December

14. ABSTRACT

15. SUBJECT TERMS

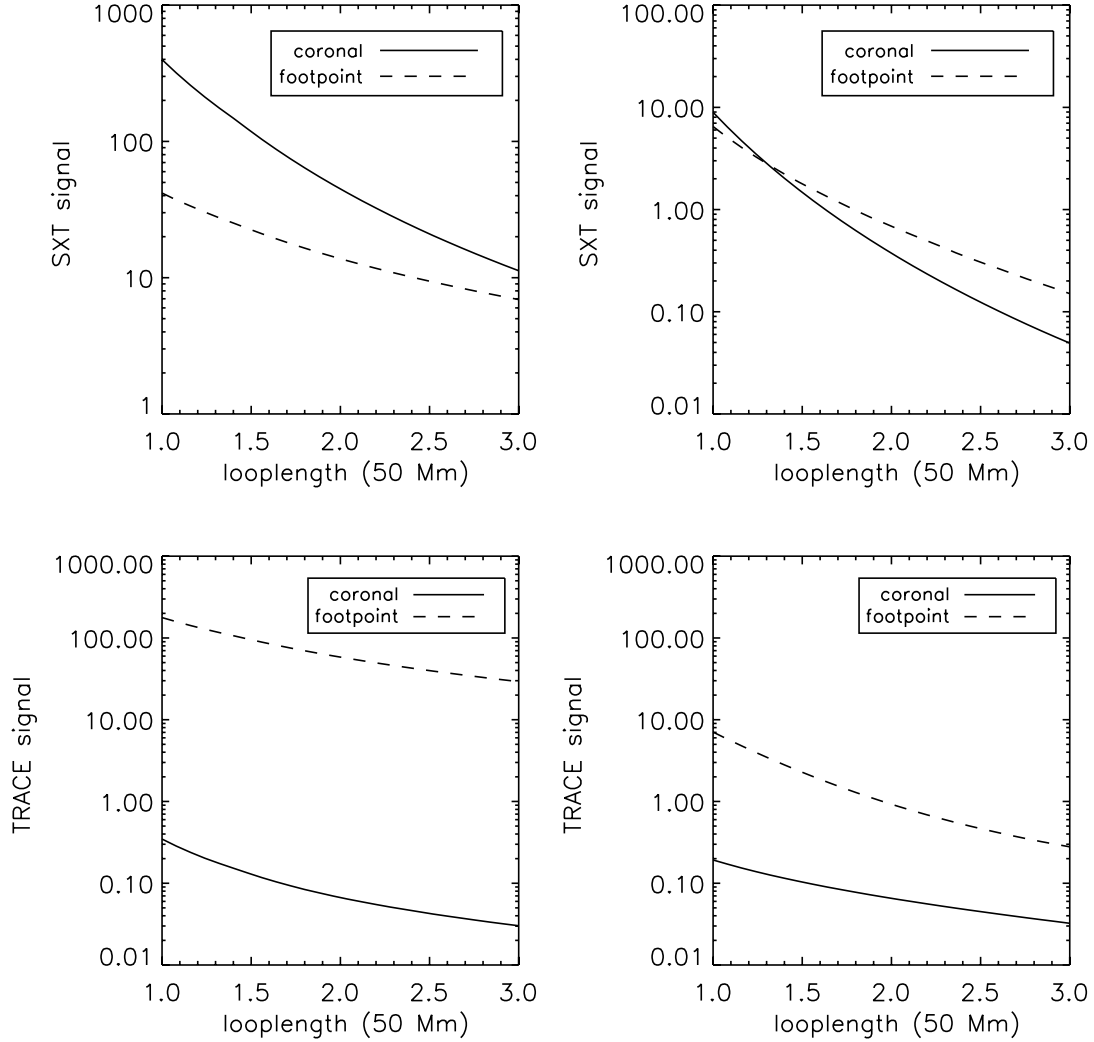| 16. SECURITY CLASSIFICATION OF:			17. LIMITATION OF ABSTRACT	18. NUMBER OF PAGES	19a. NAME OF RESPONSIBLE PERSON
a. REPORT **unclassified**	b. ABSTRACT **unclassified**	c. THIS PAGE **unclassified**	**Same as Report (SAR)**	**7**	

FIG. 1.—Variation of the intensity across the loop arcade for static equilibrium (*left*) and for impulsive heating (*right*) for SXT and *TRACE*. We plot the intensities for both the coronal (*solid line*) and transition region section (*dashed line*) of the loops. For impulsive heating the time-averaged intensities are plotted. Intensities are in units of DN pixel^{-1} s^{-1}.

calculated hydrodynamic models for 26 loops with lengths in the range 50–150 Mm, typical of observed AR loops. For the construction of the AR images we assumed that the loops have semicircular shapes and are nested one on top of the other, forming an arcade which emulates the simplest form of AR topology.

2.1. *Static Models*

We first calculated a static equilibrium AR model. The steady volumetric heating H supplied to a loop with length L was

$$H = H_0(L/L_0)^\alpha, \qquad (1)$$

with H_0 as the heating magnitude, L_0 as the length of the shortest loop, and α as a scaling-law index which depends on the details of the specific coronal heating mechanism (e.g., Mandrini et al. 2000). We chose $L_0 = 50$ Mm, $H_0 = 0.01$ ergs cm^{-3} s^{-1}, and $\alpha = -2.8$. This particular α corresponds to heating associated with the tangling of the magnetic field by photospheric convection. A nanoflare occurs when the misalignment between adjacent flux strands reaches a critical angle. Similar α-values were found to provide the best match between static models and AR and full-Sun SXR images (Warren & Winebarger 2006; Lundquist et al. 2008). In concert with these studies, H_0 was chosen so that the

temperature of the shortest and consequently hottest (according to eq. [1]) loop of the arcade was ≈4 MK, consistent with the temperature of bright SXR loops in AR cores. The DEM distributions for the coronal and footpoint sections of each simulated loop were folded with the temperature response functions of the 171 Å and AlMg channels of *TRACE* and SXT, respectively, to determine the corresponding intensities. For the calculation of the intensities we assumed that simulated loops had a diameter of 3 Mm, consistent with typical widths of observed loops.

In Figure 1 (*left*) we plot the variation of intensity across the loop arcade, while in Figure 2 (*left*) we display the corresponding synthetic images. For building the images we assume that the AR is viewed face-on, and for clarity reasons we display every fourth loop of our arcade. We applied convenient boxcars to the images to emulate the different spatial resolution of SXT (≈5″) and *TRACE* (≈1″). We assumed that the coronal emission is distributed uniformly along the loop. This is reasonable because our loops are shorter than a gravitational scale height, so there will be minimal gravitational stratification. Furthermore, the coronal temperature varies by only about 50% along most of the length of equilibrium loops (Klimchuk et al. 2008). Temperature and density of course vary dramatically in the transition region, but the
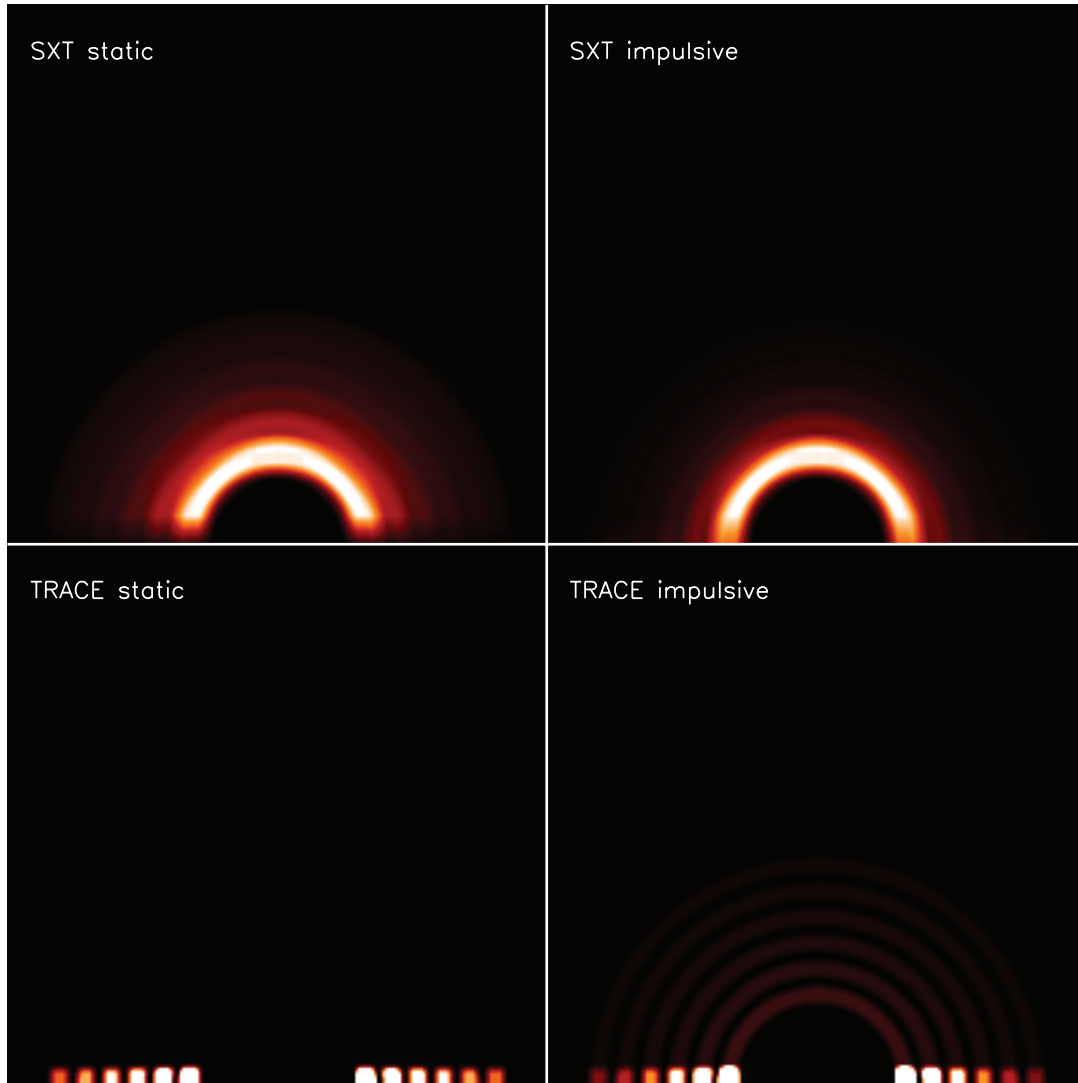
F_IG. 2.—SXT and *TRACE* images of the simulated AR loop arcade for static equilibrium (*left*) and impulsive heating (*right*). The images for the impulsive heating correspond to a time average over the corresponding simulations. It is assumed that the AR is observed face-on. The images are smoothed with boxcars consistent with the instrument resolution. The AR baseline has a length of $\approx$100 Mm. Intensity represented with color increasing from black to red to white. Each image is normalized individually.

thickness of the transition region is generally unresolvable, so we spread the emission over 2 Mm for convenience and clarity. The magnitude of the integrated transition region emission is correct.

From Figure 1 we note that the SXT emission is considerably weaker at the footpoints than in the corona. This is because the footpoint temperatures are generally below 2 MK, where SXT has greatly reduced sensitivity.

Furthermore, from Figure 2 the synthetic *TRACE* image is completely dominated by the footpoints. There is little evidence of EUV loops, which is at odds with the multitudes of EUV loops seen in the majority of observed ARs. Our results are broadly consistent with previous studies employing static heating.

Why is it that static equilibrium models fail to predict bright EUV loops together with bright SXR loops? This "pathology" is related to the fact that under static equilibrium conditions the loop temperature has a very weak dependence on the loop length. For instance, the Rosner et al. (1978) scaling law predicts that the apex temperature is related to the heating rate and length according to $T_a \propto H^{2/7}L^{4/7}$. Therefore, for the employed value $\alpha = -2.8$ we have from equation (1) that $T_a \propto L^{-0.22}$. This means that the temperature is reduced by a factor of only $3^{-0.22} = 0.8$ in

going from the shortest loop (4 MK) to the longest loop (3.1 MK) in the arcade. As shown Figure 3, our simulations closely follow the above scaling law. Therefore, none of the loops have 1–2 MK plasma in the coronal section, which is necessary to produce significant EUV emission. All of this plasma resides at the footpoints, which is where the strong *TRACE* emission originates. Obviously, we could decrease H_0 to produce strong *TRACE* emission in the corona, but then the SXT emission would be dramatically reduced. The only way to have both bright *TRACE* loops and bright SXT loops in the same arcade is for the heating rate to have a much stronger dependence on loop length. Our example arcade requires $\alpha \simeq -6$. We are not aware of any coronal heating mechanism with such an extreme dependence on L (e.g., Mandrini et al. 2000).

2.2. *Impulsive Models*

We then considered models with impulsive heating, using the same loop arcade of the previous section. We started with static equilibria having an average coronal temperature near 0.5 MK. We heated the loops with a triangular pulse lasting 50 s and let the loops cool for 8500 s, by which time the temperature had
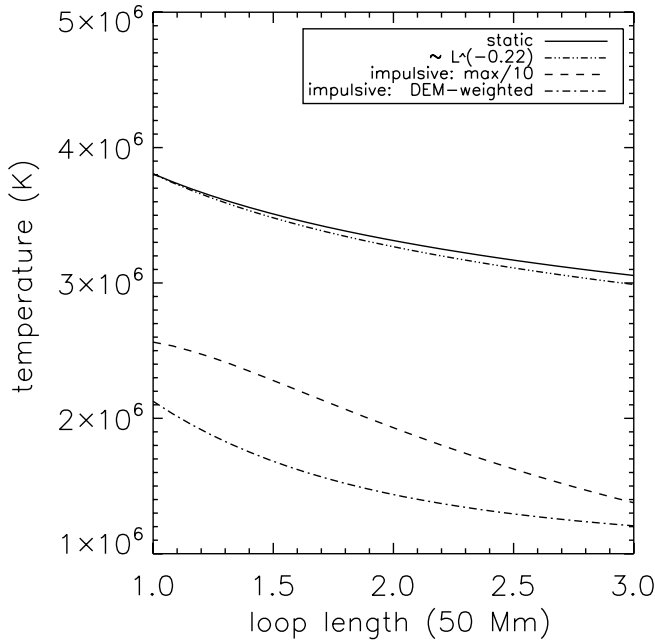
Fig. 3.—Variation of the temperature across the loop arcade. Static equilibrium model (*solid line*) and fit $\propto L^{-0.22}$ (*double-dot–dashed line*). Impulsively heated model: Maximum temperature divided by 10 (*dashed line*); DEM-weighted mean temperature (*dash-dotted line*).

cooled below 1 MK. The amplitude of the heat pulses varied from loop to loop according to equation (1), with $\alpha = -2.8$, as before, and $H_0 = 2.5$ ergs cm^{-3} s^{-1}. This produced an average DEM for the arcade that peaks near 2.0 MK, similar to that of observed ARs (e.g., Brosius et al. 1996). Each loop reaches a maximum temperature exceeding 30 MK (Fig. 3), but this happens very early in the heating event, when the density is very low. The DEM-weighted mean temperature T_{DEM} is only 1–2 MK.

We determined temporally averaged *TRACE* and SXT intensities for each loop simulation. Time averaging over the duration of a loop simulation is equivalent to taking a snapshot of a loop containing a large number of impulsively heated unresolved strands at different stages of heating and cooling. As before, we produced synthetic images of the arcade by assuming that the time-averaged intensities are uniform along each the loop. Our one-dimensional hydrodynamic simulations indicate that this is a reasonable approximation (e.g., Klimchuk et al. 2006). The right columns of Figures 1 and 2 show the intensity variation across the arcade and the synthetic image, respectively.

We note in Figure 1 that the *TRACE* emission from the footpoints is a factor of $\approx 3-100$ smaller for impulsive heating than for static heating, whereas the coronal emission is about the same in the two cases. The brightness contrast between the footpoints and corona is therefore significantly reduced for impulsive heating. This leads to a *TRACE* image in which both the coronal and footpoint emissions can be readily discerned (Fig. 2, *right*). This is not true for the static model (*left*), where the coronal emission is overwhelmed by the footpoint emission. The footpoint-to-corona intensity ratios $I_{\mathrm{foot}}/I_{\mathrm{corona}}$ are of order 10 in the impulsive model and 1000 in the static model. Observed values are in the range $\approx 2-20$. The smaller observed ratios could be due to spicular absorption of the footpoint emission (e.g., Daw et al. 1995; De Pontieu et al. 1999). Using the analytical expressions of Anzer & Heinzel (2005) for absorption at *TRACE* wavelengths and typical physical parameters of spicules given in Table 1 of Tsiropoula & Schmieder (1997) we found that attenuation factors

of the 171 *TRACE* emission of about 10 can be achieved. As a matter of fact, a recent SUMER/EIS study of moss intensities formed above and below the head of the hydrogen Lyman continuum at 912 Å demonstrated that indeed sizable absorption occurs over moss regions (B. De Pontieu et al. 2008, in preparation). Future AR models would probably need to incorporate absorption effects. Warren & Winebarger (2007) modeled an observed AR using one-dimensional simulations and also found that impulsive heating increases the visibility of EUV loops compared to static equilibrium.

It can also be seen in Figure 1 that brightness of the corona in *TRACE* relative to SXT is roughly 2 orders of magnitude larger in the impulsive model than in the static model. This suggests that bright *TRACE* loops are much more likely to be seen together with bright SXT loops in the same AR if the heating is impulsive.

The increased *TRACE*-to-SXT coronal intensity ratio and the reduced footpoint-to-corona *TRACE* contrast can both be understood as follows. In static equilibrium, the optimum temperature for a particular wave band occurs either in the corona or at the footpoints, but not at both locations. For apex temperatures >2 MK, the coronal plasma is too hot to emit appreciable *TRACE* emission, and only the footpoints are bright. This is the case for all of the loops in the static arcade. Impulsively heated loops are fundamentally different in that they experience a wide range of coronal and footpoint temperatures over the course of their evolution. When an impulsively heated loop starts to cool, *TRACE* emission occurs first at the footpoints and then over the full length of the loop when the coronal temperature drops below 2 MK. A bundle of impulsively heated strands will therefore have significant *TRACE* emission both in the corona and at the footpoints.

A final interesting property revealed in Figure 1 is the distribution of coronal emission across the arcade. SXT intensities decrease rapidly with loop length, especially in the impulsive model, while *TRACE* intensities decrease much more slowly. As a consequence, the SXT emission is concentrated in the core of the arcade, and the *TRACE* emission is much more extended (Fig. 2). This agrees well with AR observations. The strong decrease in the SXR emission with increasing L is because T_{DEM}, the dominant temperature of the plasma, drops below 2 MK for the longer loops (Fig. 3). The sensitivity of SXT is a rapidly decreasing function of temperature in this range. On the other hand, the T_{DEM} values are in the range where *TRACE* has good sensitivity, so the *TRACE* intensity gradient across the arcade is more shallow.

We then examined how the AR morphology depends on the properties of the impulsive heating. We first considered the effect of varying the index α of equation (1) by taking the following values: $-4, -3, -2$, and -1. All other aspects of the simulation were the same as for the $\alpha = -2.8$ base simulation discussed above. The resulting intensity variations across the loop arcade for *TRACE* and SXT are given in Figure 4. Not surprisingly, we found that a stronger dependence of impulsive heating on L (i.e., a more negative α) produces a steeper intensity drop-off across the arcade. Note that if we were to observe our arcade off-limb, the model with $\alpha = -1$ would yield an intensity scale height consistent with off-limb observations of the unresolved EUV corona (Cirtain et al. 2006).

The impact of the time interval between successive nanoflares, $\Delta\tau_{\mathrm{nano}}$, assuming the dependence $\Delta\tau_{\mathrm{nano}} = \Delta\tau_0(L/L_0)^\gamma$ was then examined. We consider two cases: (1) $\gamma = -2$ and $\Delta\tau_0 = 8500$ s; and (2) $\gamma = 2$ and $\Delta\tau_0 = 250$ s. For each loop we considered three consecutive nanoflares separated by $\Delta\tau_{\mathrm{nano}}$. The nanoflare heating rate and duration were the same as in the base simulation, which implies the same averaged energy per nanoflare. When $\Delta\tau_{\mathrm{nano}}$ decreases with L (case 1) the resulting images
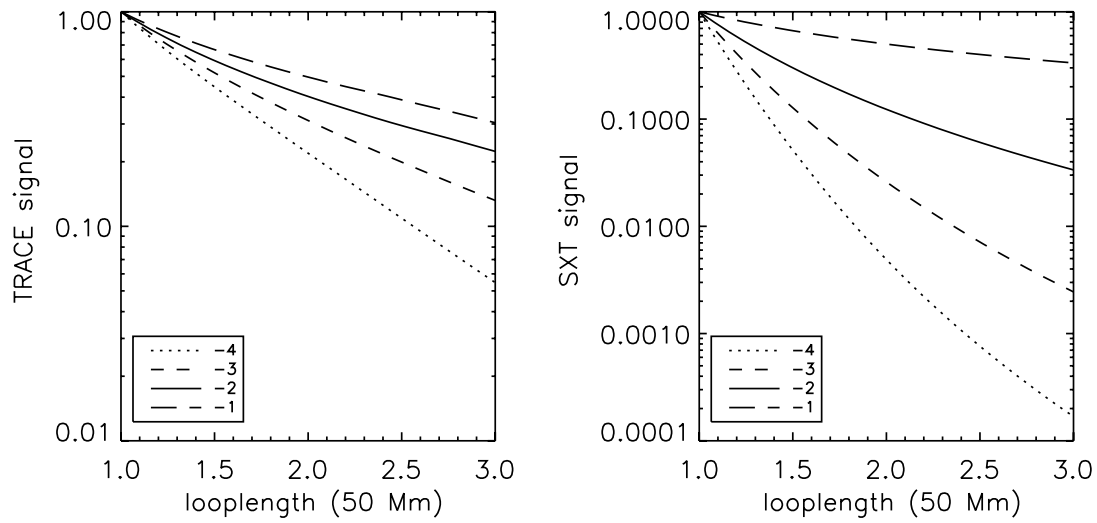
Fig. 4.—Variation of the normalized coronal intensity across the loop arcade for different values of the power-law index α, determining how the nanoflare energy is distributed across loops with different L, for *TRACE* (*left*) and SXT (*right*).
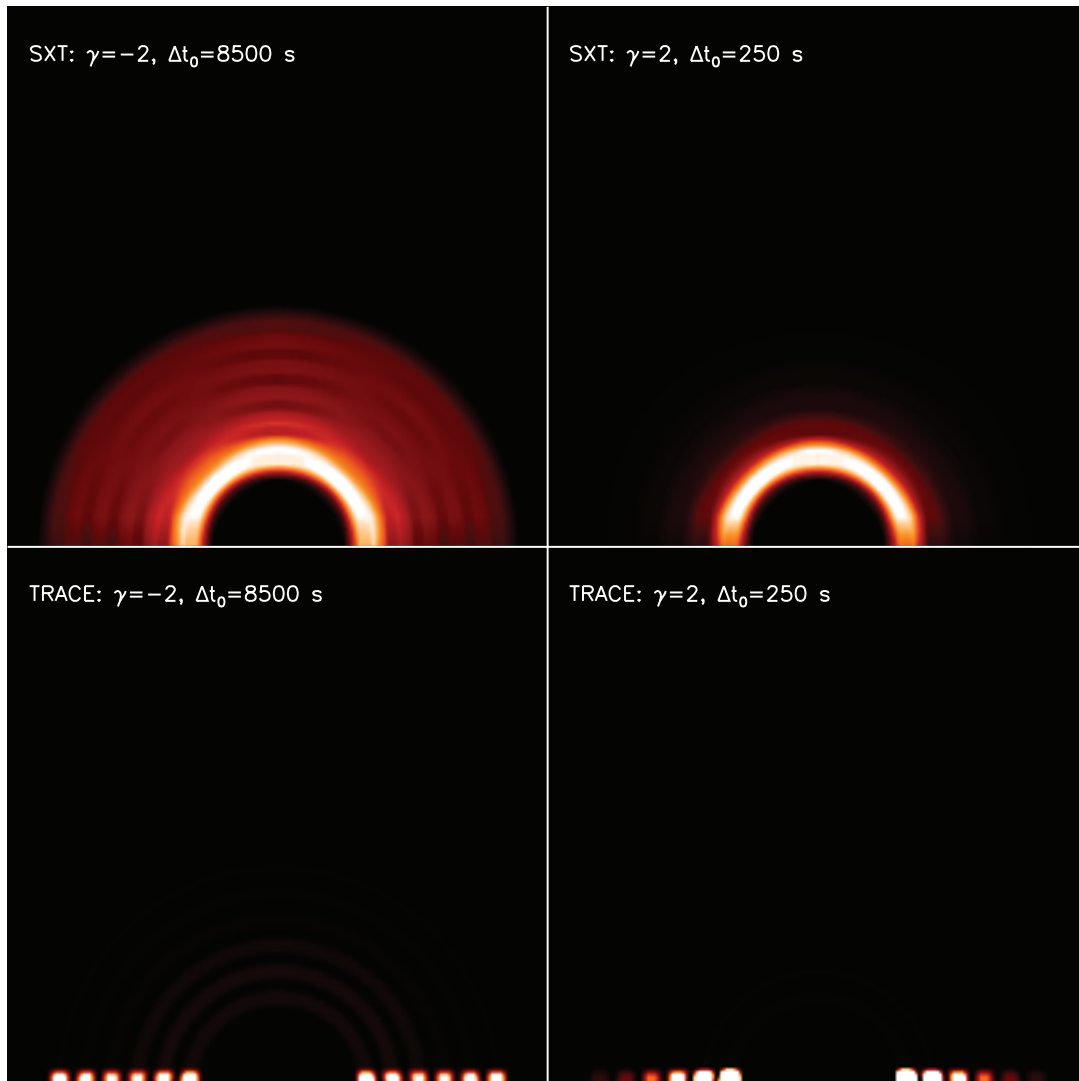

Fig. 5.—Investigating the effect of the time interval $\Delta\tau_{nano}$ between successive nanoflares. Synthetic *TRACE* and SXT images for $\Delta\tau_{nano}$ which decreases (increases) with loop length in left (right) column. The AR baseline has a length of ≈ 100 Mm. Intensity represented with color increasing from black to red to white. Each image is normalized individually.
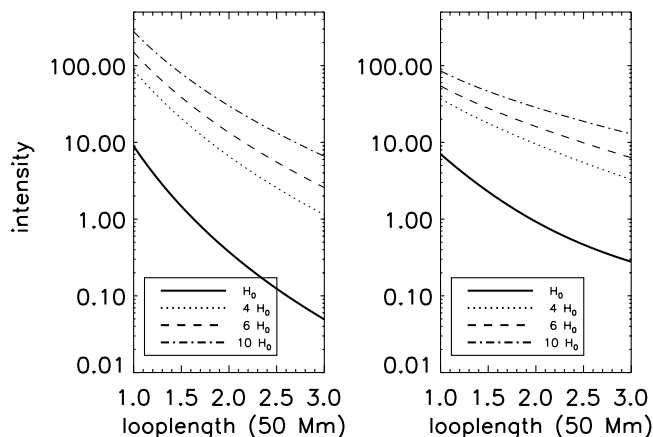
FIG. 6.—Variation of the coronal and footpoint intensity across the loop arcade for SXT (*left*) and *TRACE* (*right*), respectively, for impulsively heated AR models with different nanoflare energies. The nanoflare magnitude for each AR model are 4 (*dotted line*), 6 (*long-dashed line*), and 10 (*dash-dotted line*) times that of the base model (*solid line*). The time-averaged intensities are plotted. Intensities are in units of DN pixel^{-1} s^{-1}.

(left column of Fig. 5) are characterized by *TRACE* emission concentrated around the AR core, while the SXT emission is extended. This is because the longest loops in the arcade have $\Delta \tau_{nano}$ of about 850 s, which is not sufficient to let them cool down to *TRACE* temperatures. On the other hand, when $\Delta \tau_{nano}$ increases with L (case 2), the resulting AR images are characterized by bright core emission in SXT and lack of *TRACE* loops (right column of Fig. 5). This is because shorter loops do not have the time to cool down to *TRACE* temperatures and they remain in quasi-steady state conditions in SXT temperatures, as also shown in § 2.1. This model can explain observations of an AR with SXT loops but no *TRACE* loops (Antiochos et al. 2003).

We then investigated the effect of the magnitude of the nanoflare energy on the SXT and *TRACE* coronal and moss intensities, respectively. These intensities are particularly useful when studying the cores of ARs and can constrain the properties of the heating (e.g., Winebarger et al. 2008). On top of the base model described in the first paragraph of this section, we considered three additional AR models employing nanoflare heating magnitudes 2, 6, and 10 times the one used in the base simulation (see also eq. [1]). All other aspects of these simulations were the same as for the base simulation. The variation of the temporally averaged intensities across the loop arcade for the four models is shown in Figure 6. What can be seen in this figure is that increasing nano-

flare energy leads to higher SXT coronal-to-*TRACE* moss intensity ratio $I_{SXR}/I_{EUV\text{-}moss}$. For instance, for the inner loops in the modeled AR (i.e., its core) $I_{SXR}/I_{EUV\text{-}moss}$ increases from ≈ 1.3 to 4.4 with a 10-fold increase in the nanoflare energy. This means that $I_{SXR}/I_{EUV\text{-}moss}$ tracks in a rather sensitive way the nanoflare energy and can be used as its diagnostic. It is worth mentioning that the determined trend goes in the direction of decreasing the discrepancy with observations that can cause problems with static models. Possibly the spicular absorption discussed in the previous paragraphs could bring $I_{SXR}/I_{EUV\text{-}moss}$ to an even better agreement with the observations.

We finally found that the nanoflare duration does not alter the AR morphology for both SXT and *TRACE*. This comes as no surprise, given both instruments are mostly sensitive to the late cooling of the impulsively heated loops, when any differences in the loop response for different nanoflare durations, had been long ago smeared out (e.g., Patsourakos & Klimchuk 2005).

3. CONCLUSION

With this work we considered static and impulsive heating models of active region (AR) arcades. In concert with previous investigations, we found that static models cannot simultaneously reproduce bright EUV and SXR loops within the same AR. We showed that this is due to the shallow dependence of loop temperature on loop length implied by all reasonable coronal heating scenarios. We found that impulsive heating models agree much better with observations than do static models. In particular, impulsive heating produces (1) a reduced brightness contrast between the corona and footpoints in *TRACE* observations, (2) an increased *TRACE*-to-SXT coronal intensity ratio, and (3) enhanced SXT emission in the core of the AR and extended *TRACE* emission. We finally showed that the AR morphology depends rather sensitively on the properties of impulsive heating, such as its spatial dependence and the time interval between successive nanoflares, and can therefore be used to determine the properties of the heating. Our study paves the way for detailed comparisons between multitemperature observations of ARs and models based on impulsive heating and detailed reconstructions of the coronal magnetic field from extrapolations.

REFERENCES

Abramenko, V. I., Pevtsov, A. A., & Romano, P. 2006, ApJ, 646, L81
Antiochos, S. K., Karpen, J. T., De Luca, E. E., Golub, L., & Hamilton, P. 2003, ApJ, 590, 547
Anzer, U., & Heinzel, P. 2005, ApJ, 622, 714
Brosius, J. W., Davila, J. M., Thomas, R. J., & Monsignori-Fossi, B. C. 1996, ApJS, 106, 143
Cirtain, J., Martens, P. C. H., Acton, L. W., & Weber, M. 2006, Sol. Phys., 235, 295
Dahlburg, R. B., Klimchuk, J. A., & Antiochos, S. K. 2005, ApJ, 622, 1191
Daw, A., Deluca, E. E., & Golub, L. 1995, ApJ, 453, 929
De Pontieu, B., Berger, T. E., Schrijver, C. J., & Title, A. M. 1999, Sol. Phys., 190, 419
Katsukawa, Y., & Tsuneta, S. 2001, ApJ, 557, 343
Klimchuk, J. A. 2006, Sol. Phys., 234, 41
Klimchuk, J. A., & Karpen, J. T., & Patsourakos, S. 2007, AGU Fall Meeting (Washington: AGU), abstract SH51C-05
Klimchuk, J. A., Lopez Fuentes, M. C., & DeVore, C. R. 2006, in *SOHO*-17: Ten Years of *SOHO* and Beyond, ed. H. Lacoste & L. Ouwehand (ESA SP-617; Noordwijk: ESA), 8.1

Klimchuk, J. A., Patsourakos, S., & Cargill, P. J. 2008, ApJ, 682, 1351
Lundquist, L. L., Fisher, G. H., & McTiernan, J. M. 2008, ApJ, in press
Mandrini, C. H., Dèmoulin, P., & Klimchuk, J. A. 2000, ApJ, 530, 999
Mok, Y., Mikic, Z., Lionello, R., & Linker, J. A. 2005, ApJ, 621, 1098
———. 2008, ApJ, 679, L161
Parker, E. N. 1988, ApJ, 330, 474
Patsourakos, S., & Klimchuk, J. A. 2005, ApJ, 628, 1023
Rosner, R., Tucker, W. H., & Vaiana, G. S. 1978, ApJ, 220, 643
Schrijver, C. J., Sandman, A. W., Aschwanden, M. J., & DeRosa, M. L. 2004, ApJ, 615, 512
Tsiropoula, G., & Schmieder, B. 1997, A&A, 324, 1183
Warren, H. P., & Winebarger, A. R. 2006, ApJ, 645, 711
———. 2007, ApJ, 666, 1245
Winebarger, A. R., Warren, H. P., & Falconer, D. A. 2008, ApJ, 676, 672